SSRG International Journal of Electrical and Electronics Engineering
ISSN: 2348-8379/ https://doi.org/10.14445/23488379/IJEEE-V13I11P110

Volume 13 Issue 11, 160-173, November 2026
© 2026 Seventh Sense Research Group®

Original Article

Super-Twisting Sliding Mode Speed Control of a BLDC Hub-Motor Drive for Light Electric Vehicles with Real-Time Parameter Monitoring

Sudarshan Bhupal Gore[1], Swapnil Yashavant Gadgune[2]

[1,2]*Department of Electrical Engineering, Padmabhooshan Vasantraodada Patil Institute of Technology, Budhgaon, Sangli, Maharashtra, India.*

[1]*Corresponding Author: sudarshangore248@gmail.com*

Received: 14 October 2026 Revised: 07 November 2026 Accepted: 17 November 2026 Published: 25 November 2026

Abstract *- Brushless DC (BLDC) hub motors are widely used in light electric vehicles, but their speed response degrades when the load on the wheel or the motor parameters change. A Proportional-Integral (PI) speed loop is easy to tune, yet its disturbance rejection is limited, while a conventional first-order Sliding Mode Controller (SMC) is robust but injects high-frequency chattering into the torque command. This paper presents a second-order sliding mode speed controller for a BLDC drive based on the Super-Twisting Algorithm (STA). The sliding variable is built from the speed error and its derivative, and the control law combines a square-root term with an integral switching term, so that the control signal is continuous while finite-time convergence to the sliding surface is retained. The outer STA loop generates a torque reference that is converted to a current reference and tracked by an inner PI current loop feeding a sinusoidal PWM inverter. The complete drive is modelled in MATLAB/Simulink with a trapezoidal back-EMF machine model, and closed-loop stability is confirmed by a Lyapunov argument and by root-locus, Bode and Nyquist checks of the linearised loop. Under a 2 N·m load step, the proposed controller limits the speed dip to 1.43% against 3.78% for PI, reduces the integral absolute error by 16.5% and lowers the chattering index by 93.1% compared with the conventional SMC, with the response practically unchanged for 50% variations in stator resistance and inertia. A low-cost prototype built around an ESP32 controller, a MOSFET inverter and a 6.5-inch hub motor, with wheel speed and DC-link current monitored on an LCD and a web page, confirms the practical operation of the scheme. The results show that the super-twisting speed loop is a simple and effective option for robust speed regulation in small electric vehicle drives.*

Keywords *- Brushless DC (BLDC) motor, Chattering reduction, Electric vehicle, Lyapunov stability, Sliding Mode Control (SMC), Super-Twisting Algorithm (STA).*

1. Introduction

Electric two-wheelers, e-scooters and other Light Electric Vehicles (LEVs) are now the fastest-growing segment of electric mobility, and most of them are driven by Brushless DC (BLDC) hub motors. The BLDC motor is preferred because it gives high torque density, high efficiency and a simple commutation scheme with Hall-effect sensors [1-3]. In a hub motor, the rotor is the wheel itself, so any change in the road surface, in the gradient or in the rider load appears directly as a torque disturbance at the motor shaft. The speed controller has to keep the wheel speed close to the throttle demand in the presence of these disturbances, and it has to do so with a motor whose resistance rises with temperature and whose inertia changes with the payload.

The most common solution in commercial LEV controllers is a Proportional-Integral (PI) speed loop around a PI or hysteresis current loop [4, 5]. The PI controller is simple to tune, but its performance is tied to one operating point: when the load or the parameters move away from it, the speed dip and the recovery time under a load step grow, and re-tuning is needed [6, 7]. Several authors have therefore looked at intelligent and predictive controllers, such as fuzzy logic, neural networks, model predictive current control and tilt-integral-derivative control [5, 8-10]. These schemes improve the response, but most of them need training data, a detailed model or considerable computation, which a low-cost hub-motor controller cannot always provide.

The problem addressed in this work is therefore the regulation of the wheel speed of a hub-motor drive under sudden load torque changes and drifting motor parameters, with a control law that is light enough for a low-cost microcontroller. Sliding Mode Control (SMC) offers the required robustness, but its first-order form produces chattering in the torque command. The second-order Super-

This is an open access article under the CC BY-NC-ND license (http://creativecommons.org/licenses/by-nc-nd/4.0/)

Twisting Algorithm (STA) removes most of this chattering, yet, as the review in Section 2 shows, its use in BLDC drives has been studied mainly in simulation, without the current-limited cascade structure and the on-line monitoring that a practical LEV controller requires. This is the research gap addressed in the present work.

In this paper, a super-twisting sliding mode speed controller is designed, analysed and tested for a BLDC hub-motor drive intended for light electric vehicles. The novelty of the work is that three elements, which are not found together in earlier studies, are combined in one drive: an STA speed loop with an explicit torque-to-current conversion and a PI current loop, a stability study that uses both a Lyapunov function and frequency-domain margins, and a low-cost ESP32 prototype with real-time monitoring of speed and current.

The contribution of the work can be summarised as follows. First, a complete mathematical model of the drive is developed, covering the trapezoidal back-EMF machine, the three-phase inverter with sinusoidal PWM and the vehicle load, and a cascaded control structure is proposed in which the STA speed loop produces a torque reference that is converted to a current reference and tracked by a PI current loop. Second, the closed-loop stability of the speed loop is established with a Lyapunov function and gain conditions from the super-twisting theory, and it is cross-checked with root-locus, Bode and Nyquist analysis of the linearised loop. Third, the proposed controller is compared with a well-tuned PI controller and a conventional boundary-layer SMC on the same MATLAB/Simulink model under ramp reference, load step, reference step and parameter variation tests, using quantitative indices such as speed dip, recovery time, integral absolute error and a chattering index. Fourth, a low-cost prototype with an ESP32 controller, a MOSFET inverter, a current sensor and a 6.5-inch hub motor is built, and the wheel speed and DC-link current are monitored in real time on an LCD and a web page.

The rest of the paper is organised as follows. Section 2 reviews the related literature and states the research gap, Section 3 gives the system model, Section 4 describes the controller design and the stability analysis, Section 5 reports the simulation results, Section 6 presents the hardware prototype and its measurements, Section 7 compares the work with the existing literature and discusses the results, and Section 8 concludes the paper.

2. Literature Review

The published work on the speed control of BLDC drives can be grouped into linear, intelligent and predictive, and sliding mode methods. Review papers on BLDC machines and their control [1, 3] and on motor design for light electric vehicles [2] give the general background, and the PI regulator remains the usual choice in practical electric vehicle drives [4, 5]. Torque ripple is a second concern in these drives: Prabhu et al. reviewed its sources and the control methods used to reduce it [6], and Hari Krishna and Rajeevan proposed a multi-level voltage space vector structure for open-end winding BLDC machines for the same purpose [7].

Among the advanced controllers, Sayed et al. applied a tilt-integral-derivative regulator to an electric vehicle BLDC drive [5], İnan combined model predictive current control with an adaptive extended Kalman filter that estimates the back-EMF [8], and Prabhu et al. designed a sliding mode model predictive dual-loop controller with a self-learning strategy [10]. These methods improve the response at the cost of heavier computation or a more detailed model.

SMC is attractive for this application because it is robust to matched disturbances and parameter variations by design [11, 12]. The classical first-order SMC drives a sliding variable to zero with a discontinuous switching term, and this discontinuity, combined with the finite sampling rate and the unmodelled dynamics of the current loop, produces chattering, that is, a high-frequency oscillation in the torque command that appears as torque ripple, acoustic noise and additional losses [13, 14]. The usual remedy, a boundary layer around the surface, trades robustness for smoothness, and higher-order sliding mode control offers a better compromise. The STA proposed by Levant [15, 16] keeps the discontinuity in the derivative of the control, so the control itself is continuous, while the sliding variable still converges in finite time. Moreno and Osorio later gave a strict Lyapunov function for the STA, which allows the gains to be selected from a bound on the disturbance [17, 18], and Chalanga et al. discussed its practical implementation with observers [19].

Recent work has started to apply the STA to BLDC drives. Achdad et al. presented an adaptive STA speed controller in simulation [20], Muduli and Endla et al. used the STA inside direct torque control [21, 22], Hasni et al. compared the STA with a neural network controller [9], and Zhang et al. added a disturbance observer to a sliding mode speed loop [23]. Vadi compared PI, classical SMC, STA and an exponential reaching law SMC on a Hall-sensored BLDC motor and confirmed that the STA removes most of the chattering of the first-order SMC [14].

Similar benefits have been reported for induction and synchronous machines [13, 24, 25] and for finite-time controllers tested on low-cost hardware-in-the-loop platforms [26]. Monitoring of BLDC drives has been treated as a separate topic: Azizah et al. developed the control and monitoring of a sensorless BLDC motor with back-EMF detection [27], and Kurniawan et al. presented an open-source test bed that uses ESC telemetry [28]. From this review, the research gap between the existing methods and the present work can be stated as follows. The STA-based studies on BLDC drives are mostly limited to simulation [9, 14, 20-22];

they rarely combine the STA with an explicit torque-to-current interface and a PI current loop, so the current limit of the inverter is not part of the design; and they do not report a low-cost hardware realisation with on-line monitoring of the motor parameters, which is what a LEV controller needs. The present work is aimed at this gap, and a point-by-point comparison with the existing methods is given in Section 7.

3. System Description and Mathematical Modelling

3.1. Drive Configuration

The proposed drive is shown in Figure 1. A 48 V battery feeds a three-phase IGBT/MOSFET voltage source inverter that supplies the BLDC motor. The outer loop compares the reference speed ω_{ref} with the measured speed ω and the super-twisting controller produces the electromagnetic torque reference T_e^*. This torque reference is divided by the torque constant to obtain the current reference i^*, which is tracked by a PI current controller. The output of the current controller is the modulation signal v_c for a sinusoidal PWM generator running at 10 kHz, and the gate pulses drive the inverter. Speed and current are fed back to close the two loops. The nonlinear controller is used only where it is needed, in the speed loop that sees the load disturbance, while the current loop keeps a linear PI regulator that limits the current and protects the switches.

3.2. BLDC Motor Model

The BLDC motor has three star-connected stator windings displaced by 120° electrical and a permanent-magnet rotor. The equivalent circuit of the star-connected machine is shown in Figure 2, where each phase has a resistance, a self-inductance L, a mutual inductance M with the other phases and a back-EMF source.

Following Pillay and Krishnan [29] and Xia [30], the phase voltage equation for phase a is obtained from Kirchhoff's voltage law as

$$v_a = R_s i_a + L_s \frac{di_a}{dt} + e_a \tag{1}$$

and similar equations hold for phases b and c. Here R_s is the stator resistance, L_s is the equivalent phase inductance (self minus mutual inductance), i_a is the phase current and e_a is the back-EMF. The back-EMF is trapezoidal in shape and proportional to the rotor speed,

$$e_a = K_e F(\theta_e)\omega, \theta_e = p\theta_m \tag{2}$$

Where K_e is the back-EMF constant, $F(\theta_e)$ is a unit trapezoidal function of the electrical angle θ_e with a flat top of 120°, p is the number of pole pairs and θ_m is the mechanical rotor angle.

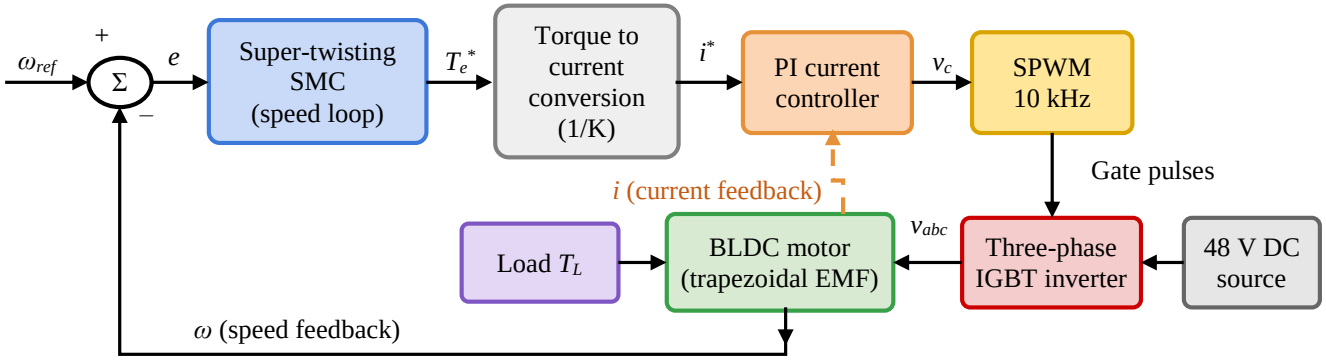

Fig. 1 Block diagram of the proposed BLDC drive with the super-twisting speed loop and the PI current loop

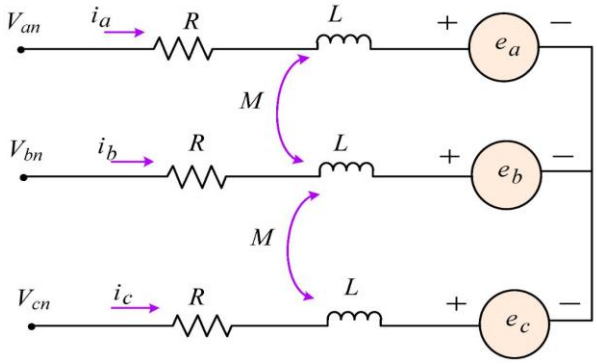

Fig. 2 Equivalent circuit of the three-phase star-connected BLDC motor with phase resistance, self and mutual inductances and trapezoidal back-EMF sources. Reproduced under the terms of the CC BY 4.0 license from Sayed et al. [5]

Equating the electrical power delivered through the back-EMF with the mechanical power gives the electromagnetic torque

$$e_a = K_e F(\theta_e)\omega, \theta_e = p\theta_m \; * \tag{3}$$

With ideal 120° commutations, only two phases conduct at any instant, and the torque simplifies to the familiar DC-motor form

$$T_e = K_t i \tag{4}$$

Where i is the DC-link (conducting phase) current and K_t is the torque constant, numerically equal to K_e in SI units. The mechanical dynamics follow Newton's law for rotation,

$$J\frac{d\omega}{dt} = T_e - T_L - B\omega, \frac{d\theta_m}{dt} = \omega \tag{5}$$

With J the total inertia referred to the motor shaft, B the viscous friction coefficient, and T_L the load torque.

Equations (1) to (5) describe the electrical and mechanical behaviour of the machine and were implemented in Simulink with the permanent magnet synchronous machine block configured for a trapezoidal flux distribution.

3.3. Inverter and PWM Model

The inverter consists of six switches arranged in three legs. Let S_a, S_b and S_c be the switching functions of the upper switches, equal to 1 when the upper switch is on and 0 when the lower switch is on.

The pole voltage of leg a with respect to the negative DC rail is $V_{dc}S_a$, and the phase voltage with respect to the star point is

$$v_{an} = V_{dc}\left(S_a - \frac{S_a+S_b+S_c}{3}\right) \tag{6}$$

With corresponding expressions for phases b and c. The switching functions are produced by a sinusoidal PWM generator in which three modulation signals, shifted by 120°, are compared with a triangular carrier at 10 kHz. The amplitude modulation index is

$$m_a = \frac{A_m}{A_c}. \tag{7}$$

Where A_m is the amplitude of the modulation signal and A_c is the carrier amplitude. In the proposed scheme, the amplitude of the modulation signal is the output v_c of the current controller, so the current loop directly sets the applied voltage.

3.4. Vehicle Load Model

For a hub motor, the motor torque is transmitted to the road through the wheel of radius r_w with a gear ratio G (equal to one for a direct-drive hub motor). The tractive force and the vehicle dynamics are

$$F_w = \frac{GT_e}{r_w}, M\frac{dv}{dt} = F_w - F_r - F_a - F_g \tag{8}$$

Where M is the vehicle mass and v the vehicle speed. The resistive forces are the rolling resistance $F_r = \mu Mg\cos\alpha$, the aerodynamic drag $F_a = \frac{1}{2}\rho C_d A v^2$ and the gradient resistance $F_g = Mg\sin\alpha$, with μ the rolling coefficient, ρ the air density, C_d the drag coefficient, A the frontal area and α the road slope. Referred to the motor shaft, these forces act as the load torque $T_L = r_w(F_r + F_a + F_g)/G$ in Equation (5), and the vehicle mass adds to the inertia J. In the simulation, the load is applied as a torque step, which is the worst case for the speed loop, and the inertia is varied to represent a change of payload.

4. Super-Twisting Sliding Mode Controller Design

4.1. Sliding Variable

The speed tracking error and the sliding variable are defined as

$$e = \omega_{ref} - \omega \tag{9}$$

$$s = \lambda e + \dot{e} \tag{10}$$

Where $\lambda > 0$ sets the slope of the sliding surface. When $s = 0$ the error obeys $\dot{e} = -\lambda e$ and decays exponentially with the time constant $1/\lambda$, whatever the load torque and the motor parameters are. The task of the controller is therefore to bring s to zero and keep it there. In practice, the derivative $\dot{e}$ is obtained from the speed measurement through a first-order low-pass filter with a 10 ms time constant, which removes the commutation ripple before differentiation.

Differentiating Equation (10) and using Equation (5) gives the dynamics of the sliding variable. The inner current loop is much faster than the speed loop, so the electromagnetic torque follows its reference through a first-order lag with time constant τ_i, that is, $\dot{T}_e = (T_e^* - T_e)/\tau_i$. Then

$$\dot{s} = \lambda\dot{e} + \ddot{e} = \varphi(t) - bu, b = \frac{1}{J\tau_i} \tag{11}$$

Where $u = T_e^*$ is the control input and $\varphi(t)$ collects the reference acceleration, the load torque derivative, the friction term and the lag of the current loop. The function $\varphi(t)$ is unknown but bounded, together with its derivative, that is, $|\dot{\varphi}| \le \Delta$ for some constant $\Delta > 0$, which is a reasonable assumption for a vehicle load. Equation (11) shows that s has relative degree one with respect to u, so a second-order sliding mode can be enforced with a continuous control [12, 15].

4.2. Control Law

The classical first-order SMC uses the discontinuous law $u = K\text{sign}(s)$, or its boundary-layer form $u = K\text{sat}(s/\phi)$ with boundary layer width ϕ [11]. Instead of this, the proposed controller uses the super-twisting algorithm [15, 18], whose block structure is shown in Figure 3. The sliding variable is split into a square-root path and a sign-integral path, and the two are summed to form the control,

$$u = k_1|s|^{1/2}\text{sign}(s) + v, \dot{v} = k_2\text{sign}(s) \qquad (12)$$

with positive gains k_1 and k_2. The first term is continuous in s and vanishes on the sliding surface, while the second term is the integral of a switching signal and is therefore also continuous. The discontinuity now appears only in $\dot{u}$, and this is why the torque reference produced by the STA is smooth compared with the first-order SMC.

The integral term also builds up the torque needed to cancel a constant load without any steady-state error, in the same way as the integral action of a PI controller, but with finite-time convergence and without the need for an accurate model. The torque reference is limited to ±8 N·m, and the current reference obtained from Equation (4) is limited to ±10 A to protect the inverter; the integrator state v is clamped at the same level to avoid wind-up.

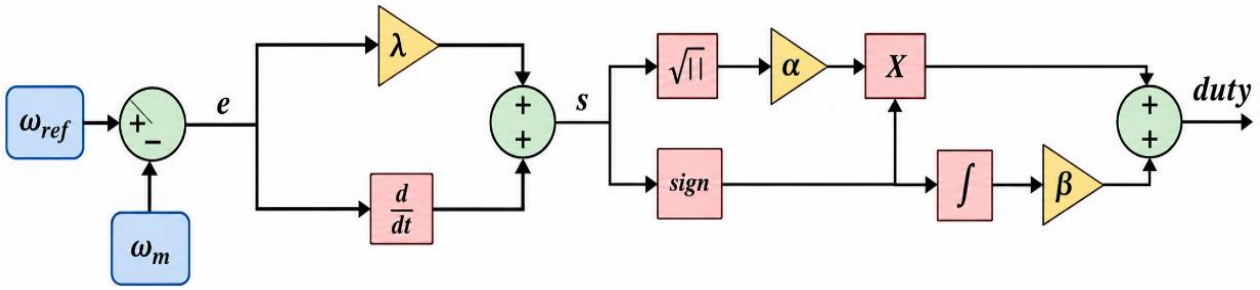

Fig. 3 Block structure of the super-twisting sliding mode speed controller: square-root path and sign-integral path acting on the sliding variable. Reproduced under the terms of the CC BY 4.0 license from Vadi [14].

4.3. Stability Analysis

Two arguments are used to show that the closed loop is stable. The first is the reaching condition. Choose the Lyapunov candidate

$$V = \frac{1}{2}s^2 \qquad (13)$$

which is positive definite. Its time derivative along Equation (11) is $\dot{V} = s\dot{s} = s(\varphi - bu)$. Substituting the control law of Equation (12) and using the bound on φ, the derivative satisfies

$$\dot{V} = s\dot{s} \le -\eta|s| < 0, \eta = bk_1|s|^{1/2} - |\varphi| > 0 \qquad (14)$$

whenever the square-root term dominates the disturbance, so V decreases and the trajectory reaches the sliding surface. Once on the surface, the error dynamics reduce to $\dot{e} = -\lambda e$, which is exponentially stable. The reaching time from an initial value $s(0)$ is bounded by

$$t_r \le \frac{|s(0)|}{\eta} \qquad (15)$$

The second argument covers the effect of the integral term and gives the gain conditions. Moreno and Osorio [17, 18] showed with a strict Lyapunov function that, for a perturbation with $|\dot{\varphi}| \le \Delta$, the origin $s = 0$, $\dot{s} = 0$ of the super-twisting dynamics is globally finite-time stable when the gains satisfy

$$k_2 > \frac{\Delta}{b}, k_1^2 \ge \frac{4\Delta(bk_2+\Delta)}{b^2(bk_2-\Delta)} \qquad (16)$$

A simpler sufficient choice often used in practice is $k_1 = 1.5\sqrt{\Delta/b}$ and $k_2 = 1.1\Delta/b$ [12]. In this work Δ was estimated from the maximum rate of change of the load torque and of the reference, the gains were first set from Equation (16) and then refined by simulation to obtain a fast load recovery with a low chattering level. The final values are $\lambda = 15$, $k_1 = 0.5$ and $k_2 = 30$. Because the conditions in Equation (16) depend only on the bound Δ and not on the exact motor parameters, the same gains remain valid when the resistance or the inertia change, which is the robustness property verified in Section 5.

4.4. Current Loop

The torque reference is converted to a current reference with the torque constant, $i^* = T_e^*/K_t$, and the current error is regulated by a PI controller,

$$v_c = K_{pi}(i^* - i) + K_{ii}\int_0^t (i^* - i)d\tau \qquad (17)$$

with $K_{pi} = 1$ and $K_{ii} = 100$. The output v_c is limited to the linear modulation range and is used as the amplitude of the three sinusoidal modulation signals of the PWM generator. With these gains, the current loop bandwidth is about 200 rad/s, which is more than ten times the bandwidth of the speed loop, so the assumption of a first-order lag used in Equation (11) holds.

5. Simulation Results and Discussion

5.1. Simulation Setup

The complete drive of Figure 1 was built in MATLAB/Simulink using Simscape Electrical blocks, as shown in Figure 4. The motor is the permanent magnet synchronous machine block with trapezoidal back-EMF, the inverter is the universal bridge with IGBT/diode switches and the PWM generator is the three-phase two-level block at 10 kHz. The model runs with a fixed step of 50 µs, which is also the sampling period of the discrete controller. The motor and drive parameters are listed in Table 1 and correspond to a 48 V hub-motor class machine; the torque constant follows from the flux linkage and the number of pole pairs. The controller parameters of the three schemes compared in this section are given in Table 2. The PI speed controller was tuned by the symmetric optimum rule and then adjusted by trial to give a critically damped response, and the conventional SMC uses the same sliding variable as the STA with a saturation function of width $\phi = 1$ rad/s so that the comparison is fair.

Table 1. Motor and drive parameters used in the simulation

Parameter	Symbol	Value
DC-link voltage	V_{dc}	48 V
Stator resistance	R_s	0.2 Ω
Stator inductance	L_s	0.5 mH
Flux linkage of magnets	ψ_m	0.1194 V·s
Pole pairs	p	4
Torque constant	K_t	0.955 N·m/A
Back-EMF constant	K_e	100 V/krpm
Rotor inertia	J	0.0027 kg·m²
Friction coefficient	B	0.00049 N·m·s/rad
PWM carrier frequency	f_c	10 kHz
Sample time	T_s	50 µs
Torque limit	T_{max}	±8 N·m
Current limit	I_{max}	±10 A

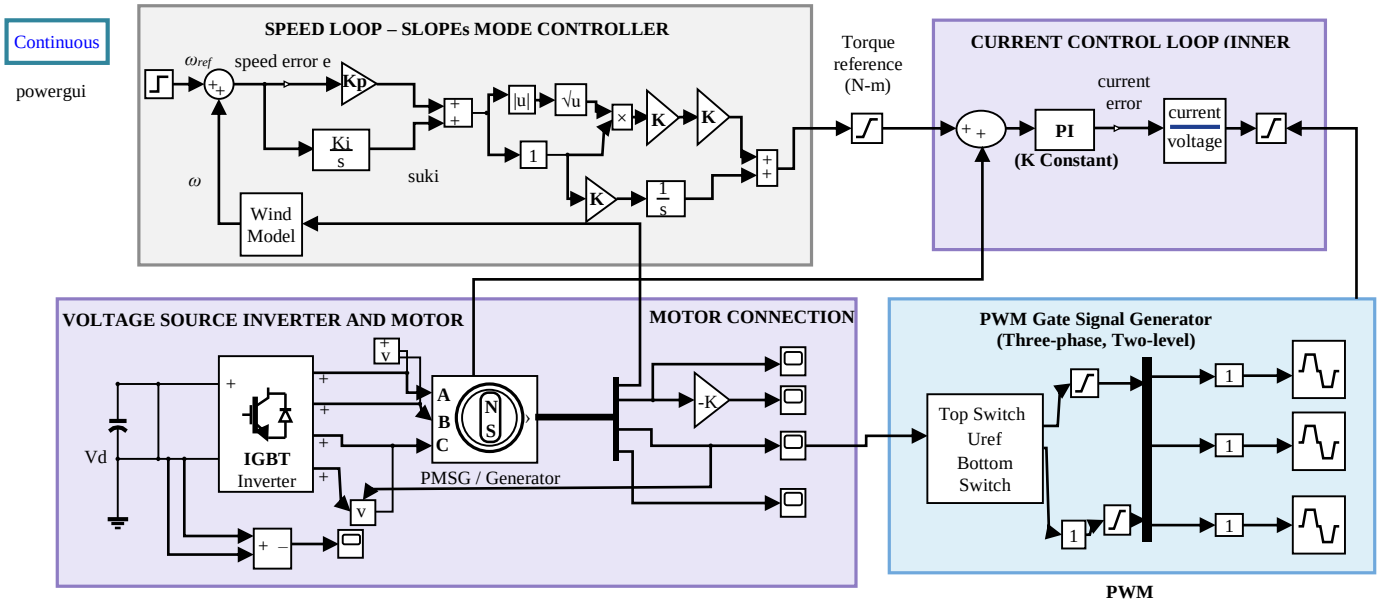

Fig. 4 MATLAB/Simulink model of the drive: Speed loop with the super-twisting controller (top left), current control loop (top right), inverter and motor (bottom left) and PWM generation (bottom right).

Table 2. Controller parameters of the three schemes

Controller	Parameter	Value
PI speed loop	K_p, K_i	1.5, 20
Conventional SMC	λ, K, ϕ	15, 6, 1 rad/s
Proposed STA-SMC	λ, k_1, k_2	15, 0.5, 30
Derivative filter	τ_f	10 ms
PI current loop	K_{pi}, K_{ii}	1, 100

The same test sequence is applied to the three controllers. The reference speed ramps from zero to 300 rpm at 50 rad/s² so that the start-up current stays within the limit, a load torque of 2 N·m is applied at 1.5 s and removed at 2.5 s, and the reference steps down to 200 rpm at 3 s. The performance is measured with the 2% settling time, the peak overshoot, the steady-state error, the speed dip under load, the recovery time to the ±0.5% band after the load step, the peak-to-peak torque and speed ripple in the loaded steady state, the integral absolute errorand a chattering index defined as the standard deviation of the torque reference in the loaded steady state,

$$\mathrm{IAE} = \int_0^T |e(t)|dt. \tag{18}$$

$$\sigma_T = \sqrt{\frac{1}{N}\sum_{k=1}^{N}\left(T_e^*[k] - T_{e,m}^*\right)^2} \quad (19)$$

where N is the number of samples in the window and $T_{e,m}^*$ is the mean torque reference. A small σ_T means a smooth control signal.

5.2. Speed Tracking and Load Disturbance

Figure 5(a) shows the speed response of the three controllers over the complete test, and Figure 5(b) zooms into the load step. All three controllers follow the ramp without a visible lag because the torque demand stays below the limit. The differences appear at the load step. The PI controller dips by 3.78% (to about 289 rpm) and takes 157 ms to return to the ±0.5% band because the integral action has to rebuild the torque slowly. The conventional SMC reacts faster and dips by only 1.64%, but it never settles: the speed keeps oscillating around a small offset of 0.25% with a peak-to-peak ripple of 0.84%, which is the chattering transmitted through the mechanical system.

The proposed STA-SMC gives the smallest dip of 1.43% and returns to the band in 81 ms with no residual oscillation and a steady-state error below 0.02%. At the reference step to 200 rpm, the PI controller undershoots by 1.97% while the STA-SMC undershoot is negligible (0.04%).

The electromagnetic torque waveforms in Figure 6 explain this behaviour. The torque of the PI drive (Figure 6(a)) is smooth but slow to rise after the load step. The conventional SMC (Figure 6(b)) switches between its limits with a peak-to-peak ripple of about 188% of the mean torque, which would produce audible noise and extra losses in a real drive. The STA-SMC torque (Figure 6(c)) rises to the 2 N·m load level almost instantly and stays close to it; the residual ripple of 13.6% comes from the derivative term reacting to the commutation ripple of the machine and is more than thirteen times smaller than that of the first-order SMC. This ripple is filtered by the inertia and does not appear in the speed, whose peak-to-peak ripple is only 0.065%. The quantitative comparison is summarised in Table 3.

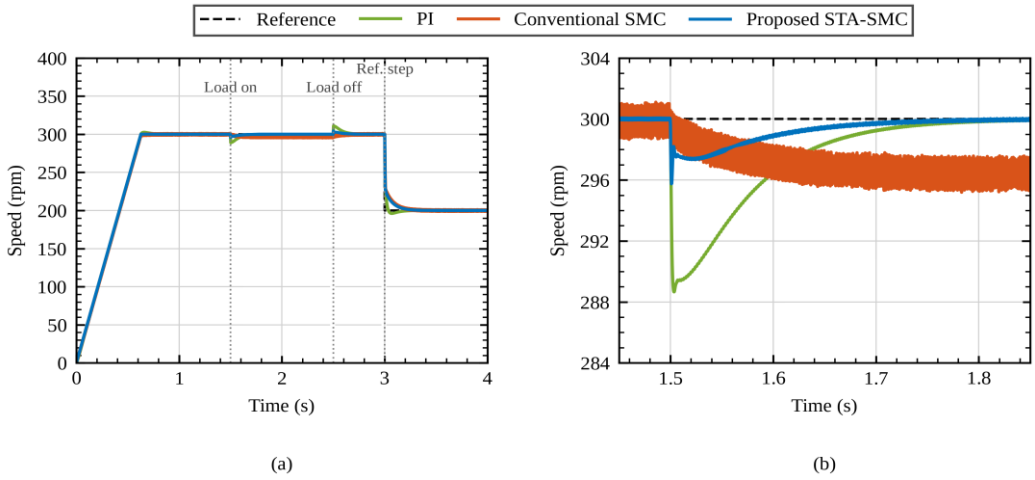

Fig. 5 Speed response of the PI, conventional SMC and proposed STA-SMC drives: (a) Complete test with ramp start, 2 N·m load step at 1.5 s, load removal at 2.5 s and reference step at 3 s, and (b) Zoom around the load application.

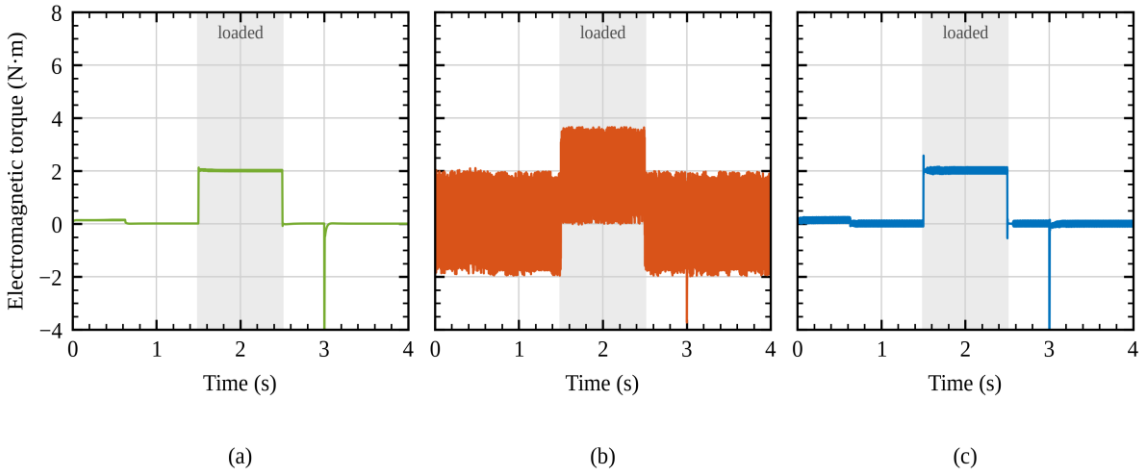

Fig. 6 Electromagnetic torque for (a) PI, (b) Conventional SMC, and (c) Proposed STA-SMC; the shaded band marks the loaded interval.

Table 3. Performance comparison of the three speed controllers (Simulation)

Index	PI	Conv. SMC	STA-SMC
2% settling time, ramp start (s)	0.62	0.62	0.62
Overshoot (%)	0.88	0.39	0.07
Steady-state error (%)	0.00	0.25	0.02
Speed dip at 2 N·m load step (%)	3.78	1.64	1.43
Recovery time to ±0.5% band (ms)	157	not reached	81
Torque ripple, loaded (%)	2.3	187.7	13.6
Speed ripple, loaded (% p-p)	0.030	0.840	0.065
Undershoot at reference step (%)	1.97	0.67	0.04
IAE (rad)	0.377	0.884	0.314
Chattering index σ_T (N·m)	0.004	5.575	0.383

5.3. Phase Current and Sliding Variable

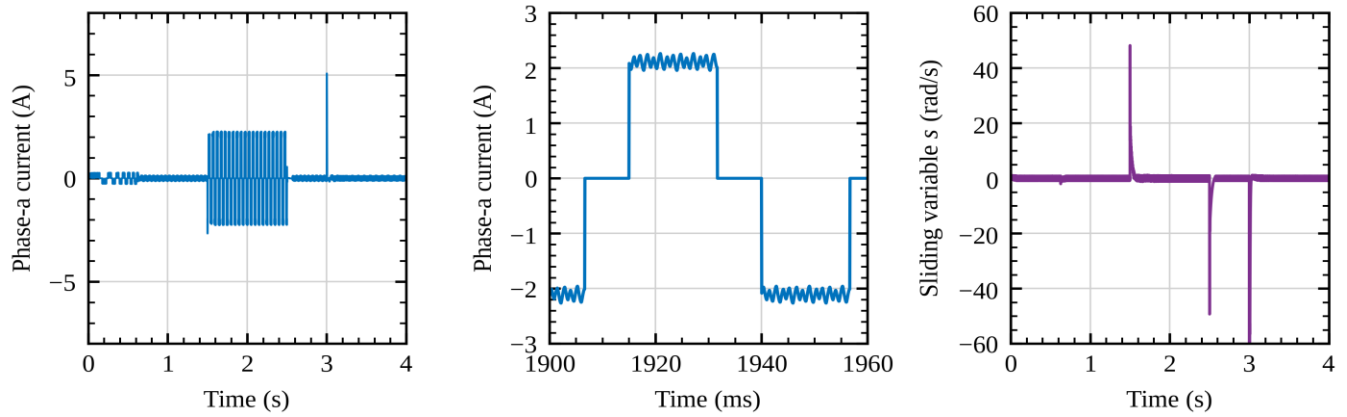

(a) (b) (c)

Fig. 7 Internal signals of the STA-SMC drive: (a) Phase-A current over the complete test, (b) Zoom of the phase-a current in the loaded steady state, and (c) Sliding variable.

Figure 7 shows the internal signals of the proposed drive. The phase-a current in Figure 7(a) is small during the no-load ramp, rises to the loaded value of about 2.1 A when the 2 N·m load is applied and shows a short peak at the reference step. The zoomed view in Figure 7(b) confirms the quasi-square 120° conduction pattern expected of a BLDC machine, with a small ripple at the switching frequency. Figure 7(c) plots the sliding variable. It leaves zero only at the three disturbance instants, reaches a peak of about 50 rad/s and is brought back to zero within a few tens of milliseconds by the square-root and integral terms, after which it stays within a narrow band. This is the finite-time reaching behaviour predicted by Equations (14) and (15), and the absence of high-frequency excursions in s follows from the continuous control law.

5.4. Robustness to Parameter Variation

To check the robustness claim of Section 4.3, the load-step test was repeated with the stator resistance increased by 50% (hot winding), the inertia increased by 50% (heavier payload) and both together, while the controller gains were kept at their nominal values. Figure 8 shows the speed around the load application and removal, and Table 4 lists the indices. The speed dip stays between 1.12% and 1.47% in all four cases, the recovery time changes by less than 15 ms and the steady-state error remains below 0.02%.

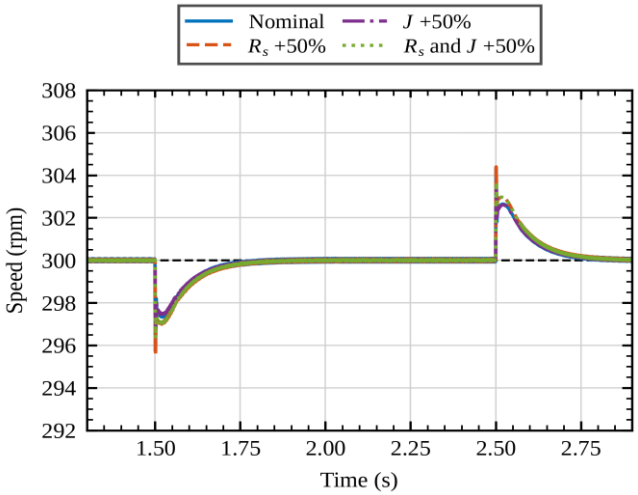

Fig. 8 Speed of the STA-SMC drive around the load step for nominal parameters and for 50% increases in stator resistance and inertia

A higher inertia actually reduces the dip because the same load torque produces a smaller deceleration, and a higher resistance is compensated by the current loop and the integral term of the STA. The four curves in Figure 8 are almost on top of each other, which is the expected behaviour of a sliding mode controller: once the trajectory is on the surface, the response is governed by λ alone and not by the plant parameters.

Table 4. Robustness of the STA-SMC drive to parameter variation

Case	Dip (%)	Recovery (ms)	Error (%)	IAE (rad)
Nominal	1.43	81	0.016	0.314
R_s + 50%	1.47	86	0.012	0.326
J + 50%	1.12	73	0.007	0.353
R_s and J + 50%	1.22	84	0.006	0.371

5.5. Performance Summary

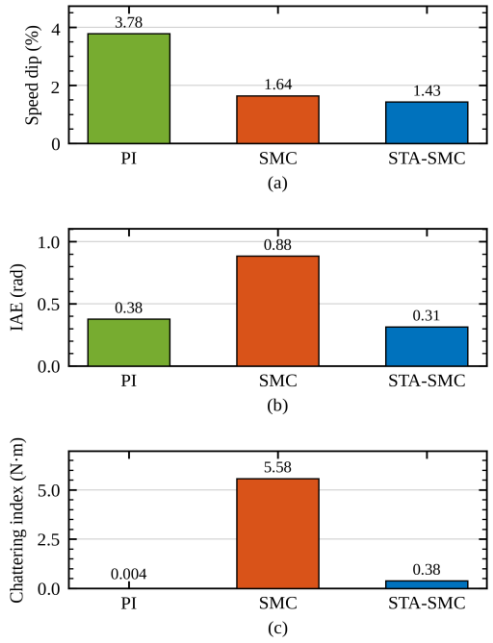

Fig. 9 Performance indices of the three controllers: (a) Speed dip under the 2 N·m load step, (b) Integral absolute error over the complete test, and (c) Chattering index of the torque reference.

Figure 9 compares the three controllers on the three indices that matter most for a vehicle drive. The speed dip under load (Figure 9(a)) is reduced from 3.78% with PI to 1.43% with the STA-SMC, a reduction of 62.3%. The integral absolute error over the complete test (Figure 9(b)) is 0.31 rad for the STA-SMC against 0.38 rad for PI and 0.88 rad for the conventional SMC. The chattering index (Figure 9(c)) drops from 5.58 N·m for the first-order SMC to 0.38 N·m for the STA-SMC, that is, by 93.1%, while remaining small enough not to affect the speed. In short, the proposed controller keeps the robustness of the sliding mode approach and the smoothness of the linear controller at the same time.

5.6. Linear Stability Checks

The Lyapunov analysis of Section 4.3 guarantees stability of the nonlinear loop. As an additional check that is familiar to drive engineers, the loop was linearised around the sliding surface. Near $s = 0$ the square-root term behaves like a proportional gain k_{eq} on s, so the speed controller becomes $C(s) = k_{eq}(\lambda + s)/(1 + \tau_f s)$ with τ_f the derivative filter time constant, and the plant is the current loop of Equation (17) in series with the mechanical transfer function $K_t/(Js + B)$.

Figure 10 shows the results for $k_{eq} = 0.03$. The pole-zero map in Figure 10(a) has all open-loop poles on the negative real axis at -0.18, -75.5, -100 and -1324 s^{-1}, and the closed-loop poles (squares) at -12.2, -100 and -694 ± j907 s^{-1}, all in the left half-plane. The root locus in Figure 10(b) stays in the left half-plane for every value of k_{eq} up to 40, so the loop cannot be destabilised by a larger equivalent gain. The Bode plots in Figures 10(d) and 10(e) give a crossover frequency of 788 rad/s, a phase margin of 63.8° and an infinite gain margin, because the phase never reaches -180°. Finally, the Nyquist plot in Figures 10(c) and 10(f) does not encircle the critical point (-1, j0), which confirms closed-loop stability by the Nyquist criterion.

These margins are well above the usual design targets of 45° and 6 dB and agree with the well-damped responses in Figures 5 to 8.

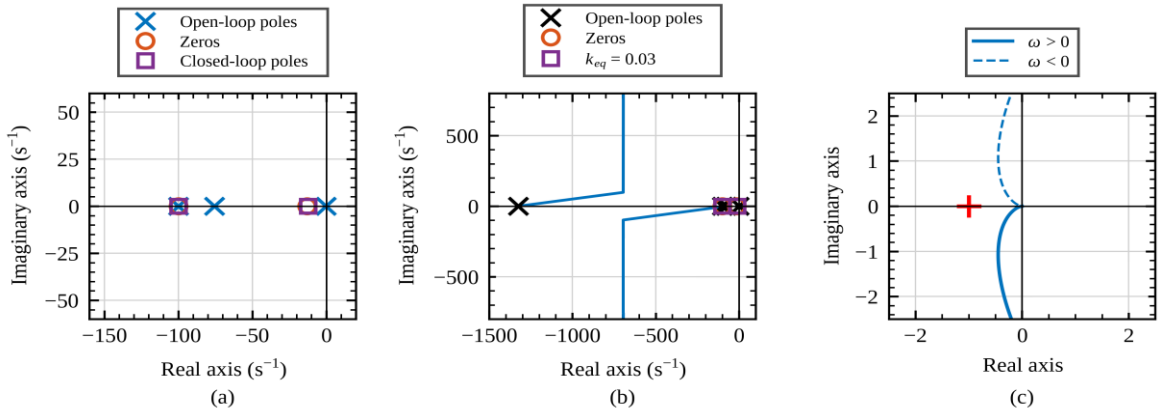

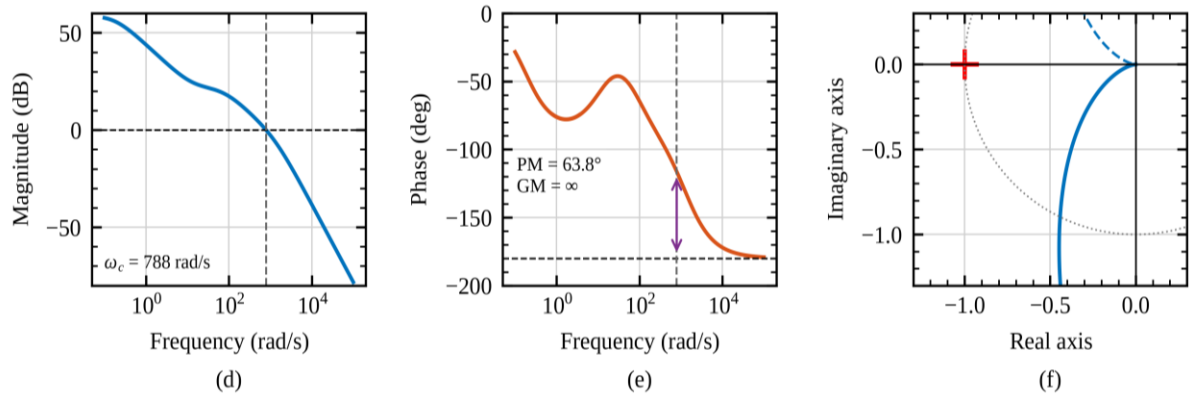

Fig. 10 Linear stability analysis of the speed loop: (a) Pole-Zero map, (b) Root locus for the equivalent gain, (c) Nyquist plot, (d) Bode magnitude and (e) Bode phase of the loop gain, and (f) Nyquist plot zoomed around the critical point.

6. Hardware Implementation and Experimental Results

6.1. Prototype Description

A low-cost prototype was built to verify that the scheme can be realised with the type of hardware found in commercial LEV controllers. It is shown in Figure 11, and its main components are listed in Table 5. The motor is a 6.5-inch direct-drive BLDC hub motor of the kind used in self-balancing scooters, with built-in Hall-effect sensors. The power stage is a three-phase MOSFET bridge assembled on a prototyping board with half-bridge gate driver ICs, bootstrap capacitors and a 5 V regulator for the logic supply. An ESP32 module runs the control program: it reads the Hall sensors to obtain the rotor position and the wheel speed, performs the commutation, runs the speed controller at a fixed sampling rate and generates the PWM signals for the gate drivers. The DC-link current is measured with a Hall-effect current sensor module, and the reference speed can be set either from a slide potentiometer (manual mode) or from a web page served by the ESP32 over Wi-Fi (web mode). An Arduino Nano drives a 20 × 4 LCD showing the operating mode, PWM duty, wheel speed and DC-link current, and the same quantities are pushed to the web page so that the drive can be monitored from a phone or a laptop.

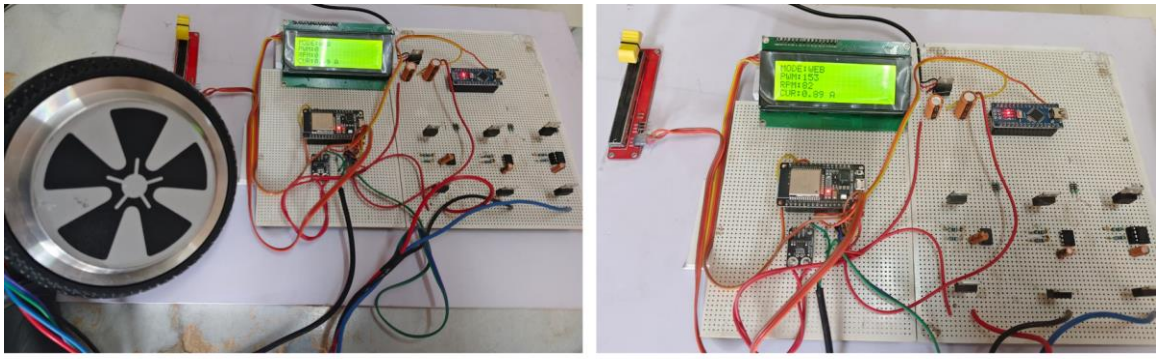

(a) **(b)**

Fig. 11 Hardware prototype: (a) Complete set-up with the 6.5-inch hub motor, ESP32 controller, current sensor, throttle slider, LCD and MOSFET inverter at standstill, and (b) Controller and inverter boards during operation in web mode at 60% duty.

Table 5. Main components of the hardware prototype

Component	Description	Function
Hub motor	6.5-inch BLDC hub motor, 36 V class, built-in Hall sensors	Traction motor and wheel
Controller	ESP32 module (dual-core, 240 MHz, Wi-Fi)	Commutation, speed control, PWM, web server
Power stage	Three-phase MOSFET bridge with half-bridge gate drivers	Inverter
Current sensor	Hall-effect current sensor module (ACS712 type)	DC-link current measurement
Display unit	Arduino Nano with 20 × 4 character LCD	Local display of mode, PWM, rpm and current
Throttle	Slide potentiometer	Manual speed reference
Auxiliary supply	5 V linear regulator with filter capacitors	Logic and driver supply

6.2. Measurements

Figure 11(a) shows the prototype at standstill: the LCD reads PWM 0, 0 rpm and a DC-link current of 0.19 A, which is the quiescent consumption of the gate drivers, the controller boards and the sensor offset. Figure 11(b) shows the drive running in web mode at a PWM value of 153 (60% duty), where the LCD reports a wheel speed of 82 rpm and a DC-link current of 0.89 A. The steady-state measurements taken at six duty-cycle settings are collected in Table 6 and plotted in Figure 12. The wheel speed is linear in the duty cycle with a slope of 1.37 rpm per percent (Figure 12(a)), as expected for a voltage-fed BLDC machine at light load, and the no-load current increases from 0.19 A to 1.45 A at full duty (Figure 12(b)) as the friction and iron losses of the hub motor grow with speed.

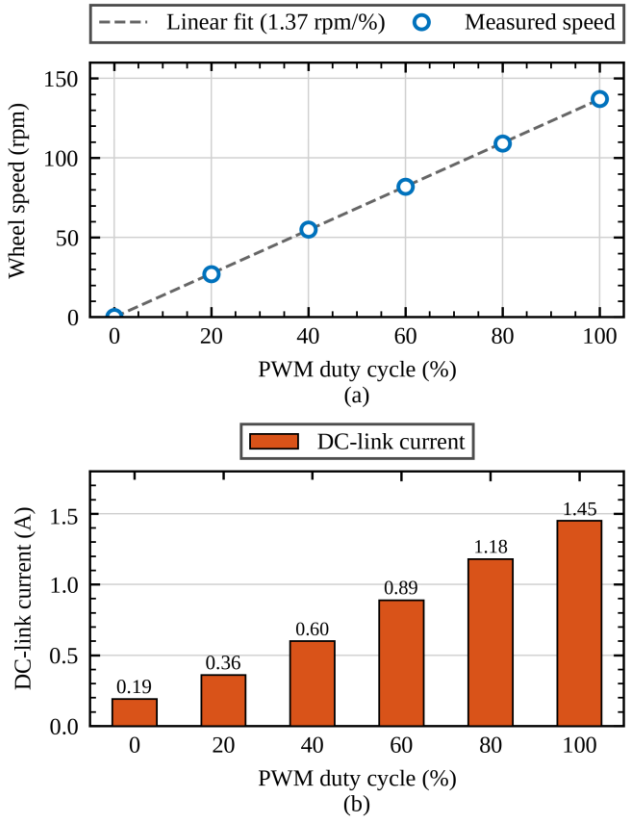

Fig. 12 Steady-state measurements on the prototype: (a) Wheel speed versus PWM duty cycle with a linear fit, and (b) DC-link current versus PWM duty cycle.

Table 6. Steady-state measurements on the prototype at no load

PWM value (0-255)	Duty cycle (%)	Wheel speed (rpm)	DC-link current (A)
0	0	0	0.19
51	20	27	0.36
102	40	55	0.60
153	60	82	0.89
204	80	109	1.18
255	100	137	1.45

During the start-up at 60% duty, the wheel reaches its final speed in about 4 s, which is set by the wheel inertia and the current limit of the prototype, and when the wheel is braked by hand, the speed reported on the LCD drops by 3 to 4 rpm (about 4%) before the controller restores it. The prototype therefore reproduces the qualitative behaviour of the simulation: a smooth start, a small dip and a recovery under load, and no audible chattering from the motor. The resolution of the Hall-based speed measurement (about 1 rpm at this speed) and the manual loading limit the accuracy of the hardware test, and a dynamometer test with a calibrated load and a logged speed transient is planned as the next step.

7. Comparison with Existing Work and Discussion

Table 7 places the present work next to recent studies on advanced speed control of BLDC and related drives. Most of the STA-based works are validated in simulation only [9, 14, 20-22], and those with hardware use a DSP or hardware-in-the-loop platform [5, 26].

The proposed scheme differs in three ways. It uses the STA in the speed loop with an explicit torque-to-current conversion and a PI current loop, which keeps the current limit and the inverter protection in the linear part of the controller; it reports the stability with both a Lyapunov proof and frequency-domain margins; and it demonstrates the controller together with real-time monitoring of speed and current on a low-cost ESP32 platform driving an actual hub motor. The quantitative improvement over PI in speed dip and over conventional SMC in chattering is in line with, or better than, the values reported for similar drives [13, 14], with the advantage that the algorithm needs only three gains and no training data or observer.The reasons for the improvement can be traced to the structure of the control law. With respect to the PI controller, the sliding variable contains the derivative of the speed error, and the square-root term of Equation (12) has a high gain near the sliding surface, so the torque reference responds to a load step as soon as the speed begins to fall, whereas the PI integrator needs time to build up the same torque.

This explains the smaller speed dip (1.43% against 3.78%) and the shorter recovery time (81 ms against 157 ms). With respect to the conventional SMC, the switching action of the STA is placed behind an integrator, so the torque reference is continuous, and the chattering index falls from 5.58 N·m to 0.38 N·m, while the integral term removes the 0.25% offset left by the boundary layer. The gain conditions of Equation (16) depend on the bound of the disturbance and not on the motor parameters, which is why the response is nearly the same for 50% changes in resistance and inertia. Finally, the cascaded structure leaves the current limit in the PI current loop, so the improvement in the speed loop is obtained within the ratings of the inverter.

Table 7. Comparison of the present work with recent studies on advanced speed control of BLDC drives

Reference	Controller	Machine/application	Validation	Load and parameter tests	On-line monitoring
Sayed et al. [5]	Tilt-integral-derivative	BLDC, electric vehicle	Simulation and test bench	Load step	No
Achdad et al. [20]	Adaptive STA	BLDC	Simulation	Load step	No
Muduli [21]	Optimised STA in DTC	BLDC	Simulation	Load step	No
Hasni et al. [9]	ANN versus STA	BLDC	Simulation	Reference change	No
Prabhu et al. [10]	Sliding mode MPC, self-learning	BLDC, electric vehicle	Simulation	Load step	No
Vadi [14]	PI, SMC, STA, ERL-SMC	Hall-sensored BLDC	Simulation	Load, voltage, reference	No
Iqbal [26]	Finite-time stability controllers	BLDC	Simulation and STM32 HIL	Initial conditions	No
This work	STA speed loop with PI current loop	BLDC hub motor, light EV	Simulation and ESP32 prototype	Load step, R_s and J variation, reference step	LCD and web page

8. Conclusion

This paper has presented a super-twisting sliding mode speed controller for a BLDC hub-motor drive intended for light electric vehicles. The drive was modelled completely, from the trapezoidal back-EMF machine and the PWM inverter to the vehicle load, and a cascaded structure was proposed in which the STA speed loop sets a torque reference that is tracked by a PI current loop. The stability of the loop was established with a Lyapunov function and gain conditions from the super-twisting theory, and confirmed by root-locus, Bode and Nyquist analysis, which gave a phase margin of 63.8° and an infinite gain margin.

In simulation, the proposed controller reduced the speed dip under a 2 N·m load step from 3.78% (PI) to 1.43%, cut the integral absolute error by 16.5% and lowered the chattering index by 93.1% with respect to a conventional sliding mode controller, while the response remained practically unchanged for 50% variations in stator resistance and inertia. A low-cost ESP32-based prototype with a 6.5-inch hub motor confirmed smooth operation with a small speed dip under load and provided real-time monitoring of speed and current on an LCD and a web page. Future work will add a dynamometer load with logged transients, a sliding mode observer for sensorless speed estimation, and an adaptive adjustment of the super-twisting gains to reduce the residual torque ripple at high speed.

Conflicts of Interest

The authors declare that there is no conflict of interest regarding the publication of this paper.

Funding Statement

This research received no specific grant from any funding agency in the public, commercial or not-for-profit sectors.

Acknowledgments

The authors thank the Department of Electrical Engineering, Padmabhooshan Vasantraodada Patil Institute of Technology, Budhgaon, for providing the laboratory facilities used to build and test the hardware prototype.

References

[1] Deepak Mohanraj et al., "A Review of BLDC Motor: State of Art, Advanced Control Techniques, and Applications," *IEEE Access*, vol. 10, pp. 54833-54869, 2022. [CrossRef] [Google Scholar] [Publisher Link]

[2] Zbigniew Gmyrek, "Optimal Electric Motor Designs of Light Electric Vehicles: A Review," *Energies*, vol. 17, no. 14, pp. 1-35, 2024. [CrossRef] [Google Scholar] [Publisher Link]

[3] Suhair Akram, and Mohanned Aljanabi, "A Comprehensive Investigation of Brushless Direct Current (BLDC) Motors: Current State, Advanced Control Strategies, and Utilization Systems," *Salud, Ciencia y Tecnología-Serie de Conferencias*, vol. 3, pp. 1-15, 2024. [CrossRef] [Google Scholar] [Publisher Link]

[4] Sandipan Pine, and Bibhuti Bhusan Choudhury, "Design Strategy and Implementation of Control Parameters for BLDC Motor Application in an Electric Vehicle," *International Journal of Electrical Engineering and Computer Science*, vol. 6, pp. 36-45, 2024. [CrossRef] [Google Scholar]

[5] Khairy Sayed et al., "Application of Tilt Integral Derivative for Efficient Speed Control and Operation of BLDC Motor Drive for Electric Vehicles," *Fractal and Fractional*, vol. 8, no. 1, pp. 1-25, 2024. [CrossRef] [Google Scholar] [Publisher Link]

[6] Nagesh Prabhu, R. Thirumalaivasan, and Bragadeshwaran Ashok, "Critical Review on Torque Ripple Sources and Mitigation Control Strategies of BLDC Motors in Electric Vehicle Applications," *IEEE Access*, vol. 11, pp. 115699-115739, 2023. [CrossRef] [Google Scholar] [Publisher Link]

[7] U. Hari Krishna, and P.P. Rajeevan, "Multi-Level Voltage Space Vector Structure based Control Strategy with Reduced Torque Ripple for Open-End Winding BLDC Motor Drives," *IEEE Access*, vol. 12, pp. 74524-74538, 2024. [CrossRef] [Google Scholar] [Publisher Link]

[8] Remzi Inan, "An Improved Model Predictive Current Control of BLDC Motor with a Novel Adaptive Extended Kalman Filter-based Back EMF Estimator and a New Commutation Duration Approach for Electrical Vehicle," *International Journal of Circuit Theory and Applications*, vol. 53, no. 2, pp. 1135-1150, 2025. [CrossRef] [Google Scholar] [Publisher Link]

[9] Anwar Hasni et al., "Optimized Speed Regulation of BLDC Motors: A Comparative Performance Study of Artificial Neural Networks and Super-Twisting Sliding Mode Controllers," *International Journal of Robotics and Control Systems*, vol. 5, no. 4, pp. 2360-2378, 2025. [CrossRef] [Google Scholar] [Publisher Link]

[10] N. Prabhu, Thirumalaivasan Rajaram, and Bragadeshwaran Ashok, "Design of Sliding Mode Model Predictive Dual-Loop Control through Self-Learning Strategy to Mitigate the Torque Ripple in BLDC Motor for Electric Vehicles," *Scientific Reports*, vol. 15, no. 1, pp. 1-16, 2025. [CrossRef] [Google Scholar] [Publisher Link]

[11] Vadim Utkin, "Variable Structure Systems with Sliding Modes," *IEEE Transactions on Automatic Control*, vol. 22, no. 2, pp. 212-222, 1977. [CrossRef] [Google Scholar] [Publisher Link]

[12] Yuri Shtessel et al., *Sliding Mode Control and Observation*, 1st ed., Birkhäuser New York, NY, 2014. [CrossRef] [Google Scholar] [Publisher Link]

[13] David Marcos-Andrade et al., "Sliding Mode Speed Control in Synchronous Motors for Agriculture Machinery: A Chattering Suppression Approach," *Agriculture*, vol. 14, no. 5, pp. 1-25, 2024. [CrossRef] [Google Scholar] [Publisher Link]

[14] Seyfettin Vadi, "Robust Controller Design based on Sliding Mode Control Strategy with Exponential Reaching Law for Brushless DC Motor," *Mathematics*, vol. 14, no. 2, pp. 1-30, 2026. [CrossRef] [Google Scholar] [Publisher Link]

[15] Arie Levant, "Sliding Order and Sliding Accuracy in Sliding Mode Control," *International Journal of Control*, vol. 58, no. 6, pp. 1247-1263, 1993. [CrossRef] [Google Scholar] [Publisher Link]

[16] Arie Levant, "Robust Exact Differentiation Via Sliding Mode Technique," *Automatica*, vol. 34, no. 3, pp. 379-384, 1998. [CrossRef] [Google Scholar] [Publisher Link]

[17] Jaime A. Moreno, and Marisol Osorio, "A Lyapunov Approach to Second-Order Sliding Mode Controllers and Observers," *2008 47th IEEE Conference on Decision and Control*, Cancun, Mexico, pp. 2856-2861, 2008. [CrossRef] [Google Scholar] [Publisher Link]

[18] Jaime A. Moreno, and Marisol Osorio, "Strict Lyapunov Functions for the Super-Twisting Algorithm," *IEEE Transactions on Automatic Control*, vol. 57, no. 4, pp. 1035-1040, 2012. [CrossRef] [Google Scholar] [Publisher Link]

[19] Asif Chalanga et al., "Implementation of Super-Twisting Control: Super-Twisting and Higher Order Sliding-Mode Observer-based Approaches," *IEEE Transactions on Industrial Electronics*, vol. 63, no. 6, pp. 3677-3685, 2016. [CrossRef] [Google Scholar] [Publisher Link]

[20] R. Achdad et al., "Adaptive Super-Twisting Sliding Mode Control of a BLDC Motor Speed Control," *2024 18th International Conference on Control, Automation, Robotics and Vision*, Dubai, United Arab Emirates, pp. 1-6, 2024. [CrossRef] [Google Scholar] [Publisher Link]

[21] Utkal Ranjan Muduli, "Optimized Super Twisting Sliding Mode based Direct Torque Control for BLDC Motor," *2024 IEEE International Conference on Power Electronics, Drives and Energy Systems*, Mangalore, India, pp. 1-6, 2024. [CrossRef] [Google Scholar] [Publisher Link]

[22] Purushotham Endla et al., "Super Twisting Sliding Mode Controllers based Direct Torque Control of BLDC Motor," *2025 IEEE 2nd International Conference on Information Technology, Electronics and Intelligent Communication Systems*, Bangalore, India, pp. 1-8, 2025. [CrossRef] [Google Scholar] [Publisher Link]

[23] Xing-guo Zhang et al., "A Disturbance Observer based Sliding Mode Controller for BLDC Motors," *Journal of Physics: Conference Series*, vol. 3074, no. 1, pp. 1-8, 2025. [CrossRef] [Google Scholar] [Publisher Link]

[24] Sadia Ali, Alvaro Prado, and Mahmood Pervaiz, "Hybrid Backstepping-Super Twisting Algorithm for Robust Speed Control of a Three-Phase Induction Motor," *Electronics*, vol. 12, no. 3, pp. 1-27, 2023. [CrossRef] [Google Scholar] [Publisher Link]

[25] Saad Kelam, Rachida Hadiby Ghoul, and Mohammed Belkheiri, "Super-Twisting Sliding Mode Control of Induction Motor," *International Journal on Electrical Engineering and Informatics*, vol. 17, no. 3, pp. 533-548, 2025. [CrossRef] [Google Scholar] [Publisher Link]

[26] Arif Iqbal, "Finite-Time Stability-based Chaos Suppression of Brushless DC Motor," *Engineering Research Express*, vol. 8, no. 3, 2026. [CrossRef] [Google Scholar] [Publisher Link]

[27] Nada Syadza Azizah, Feri Adriyanto, and Joko Slamet Saputro, "Development of Control and Monitoring of BLDC Motor Speed without Sensor with Back EMF Detection," *Journal of Electrical, Electronic, Information, and Communication Technology*, vol. 5, no. 1, pp. 1-9, 2023. [CrossRef] [Google Scholar] [Publisher Link]

[28] Uun Triyas Yuni Kurniawan, Faridah, and Sunarno, "An Open-Source BLDC Motor Test Bed Utilizing ESC Telemetry for Cost-Effective Educational Laboratories," *HardwareX*, vol. 26, pp. 1-22, 2026. [CrossRef] [Google Scholar] [Publisher Link]

[29] Pragasen Pillay, and R. Krishnan, "Modeling, Simulation, and Analysis of Permanent-Magnet Motor Drives II: The Brushless DC Motor Drive," *IEEE Transactions on Industry Applications*, vol. 25, no. 2, pp. 274-279, 1989. [CrossRef] [Google Scholar] [Publisher Link]

[30] Chang-liang Xia, *Permanent Magnet Brushless DC Motor Drives and Controls*, John Wiley and Sons, 2012. [Google Scholar] [Publisher Link]